**Rama Aravind Prabhakaran**[1]
**Yilong Zhou**[1]
**Saurin Patel**[1]
**Akshay Kale**[1]
**Yongxin Song**[2]
**Guoqing Hu**[3]*
**Xiangchun Xuan**[1]

[1]Department of Mechanical Engineering, Clemson University, Clemson, SC, USA
[2]College of Marine Engineering, Dalian Maritime University, Dalian, P. R. China
[3]LNM, Institute of Mechanics, Chinese Academy of Sciences, Beijing, P. R. China

Received June 24, 2016
Revised August 16, 2016
Accepted August 17, 2016

Research Article

# Joule heating effects on electroosmotic entry flow

Electroosmotic flow is the transport method of choice in microfluidic devices over traditional pressure-driven flow. To date, however, studies on electroosmotic flow have been almost entirely limited to *inside* microchannels. This work presents the first experimental study of Joule heating effects on electroosmotic fluid entry from the inlet reservoir (i.e., the well that supplies fluids and samples) to the microchannel in a polymer-based microfluidic chip. Electrothermal fluid circulations are observed at the reservoir-microchannel junction, which grow in size and strength with the increasing alternating current to direct current voltage ratio. Moreover, a 2D depth-averaged numerical model is developed to understand the effects of Joule heating on fluid temperature and flow fields in electrokinetic microfluidic chips. This model overcomes the problems encountered in previous unrealistic 2D and costly 3D models, and is able to predict the observed electroosmotic entry flow patterns with a good agreement.

**Keywords:**
Electrokinetic / Electroosmosis / Electrothermal flow / Entry flow / Joule heating
DOI 10.1002/elps.201600296

Additional supporting information may be found in the online version of this article at the publisher's web-site

## 1 Introduction

Electrokinetics (direct current (DC) [1] and/or alternating current (AC) [2, 3]) is an efficient technique to manipulate fluids and samples (e.g., ions, molecules, viruses and cells) in microfluidic devices [4–7]. It transports fluids by electroosmosis and (charged) samples by electrophoresis through microchannels. Electroosmotic flow has a nearly plug-like velocity profile and hence produces much smaller sample dispersion than the traditional parabolic pressure-driven flow [8]. To date electrokinetic transport phenomena have been investigated on a variety of microchannel structures including straight, curved, and network of channels [9–11]. However, these studies have been almost entirely focused upon the fluid and sample transport *inside* the microchannel. Very little attention has been given to the fluid and sample entry from the inlet reservoir (i.e., the well that supplies liquids and samples) to the microchannel [12, 13]. At this interface there exists a significant mismatch in the size of the macroscale reservoir (typically a few millimeters in diameter and depth) and the microscale channel (typically tens of micrometers in width and depth). Strong electric field gradients are therefore inherently induced at the reservoir-microchannel junction [14], which have been recently demonstrated by our group to focus, trap, and sort particles via reservoir-based dielectrophoresis (rDEP) [15, 16] and/or induced charge electroosmosis [17].

Joule heating is an inevitable phenomenon accompanying electrokinetic fluid and sample transport in microfluidic devices [18]. It causes temperature rises and gradients in the fluid, and in turn draws nonuniformities into the fluid properties (e.g., electric conductivity, dielectric permittivity, and dynamic viscosity) due to their temperature dependences [19, 20]. As such, the favored plug-like velocity profile of electroosmotic flows can be distorted, which affects both the accuracy and efficiency of electrokinetic sample manipulation [21, 22]. These Joule heating effects can become significant especially when a buffer solution of high electric conductivity (which is often necessary for biosamples [23]) and/or a polymer-based (e.g. PDMS) microchip of low thermal conductivity is used [24].

Previous studies on Joule heating and its effects on electroosmotic flows have been limited to *inside* either standalone capillaries or on-chip microchannels [18–22]. In capillary electrophoresis (CE) Joule heating has been long known

**Correspondence**: Professor Xiangchun Xuan, Department of Mechanical Engineering, Clemson University, Clemson, SC 29634-0921, USA
**E-mail**: xcxuan@clemson.edu
**Fax**: +1-864-656-7299

**Abbreviations: AC**, alternating current; **DC**, direct current; **rDEP**, reservoir-based dielectrophoresis

*Additional corresponding author: Dr. Guoqing Hu
**E-mail:** guoqing.hu@imech.ac.cn.

**Colour Online:** See the article online to view Figs. 1, 3 –6 in colour.

to generate transverse gradients in fluid temperature within the capillary, which increases the hydrodynamic dispersion of sample species via nonuniform diffusion and electrophoresis [25–27]. Axial temperature gradients can occur in thermostated CE because of the dissimilar heat transfer conditions inside and outside the thermostated cartridge [28]. They can also occur near the capillary ends due to the liquid cooling effects from the reservoirs [29]. In either circumstance the axial temperature gradients have been demonstrated to induce a pressure-driven flow *inside* the capillary, leading to a reduced plate height in CE [28–30].

In electrokinetic microfluidic chips, Joule heating extends from within the fluid to the whole device due to thermal diffusion [31, 32], which significantly complicates the problem of the coupled fluid and thermal transport [33–35]. Moreover, under appropriate conditions, the action of electric field on the thermally induced gradients in fluid properties can generate a pair of counterrotating fluid vortices *inside* on-chip microchannels [36]. This so-called electrothermal flow [37, 38] was first predicted by Hawkins et al. [39] to occur near a 2D constriction in channel depth of insulator-based DEP systems. It was later experimentally verified by Sridharan et al. [36] using a rectangular microchannel with a widthwise constriction in the middle. Moreover, a 2D numerical model was developed by Sridharan et al. [36] to simulate the effects of Joule heating on electroosmotic flows in such a microfluidic chip. However, an unrealistically large convective heat transfer coefficient had to be assumed because most of the heat generated in the fluid was actually rejected along the depth-wise direction [24]. Hence, a 3D full-scale numerical model was later developed by Kale et al. [40] to capture the heat dissipation in all directions without any assumption, which, however, is computationally very expensive.

We present in this work the first experimental study of electroosmotic fluid entry from reservoir to microchannel in a PDMS-based microchip. DC-biased AC electric field is employed to drive the flow considering the increasing use of this combined electric field in recent applications [14, 39–42]. More importantly, we develop a 2D depth-averaged numerical model to study the effects of Joule heating on electroosmotic entry flows. This full-scale simulation in the horizontal plane of the microchip accounts for the influences of the top and bottom microchannel walls on the heat and fluid transfer via additional terms in the standard transport equations. It requires neither the assumption of high convective heat transfer coefficient in a regular 2D model [36] nor the consumption of expensive computational resource in a 3D model [40].

## 2 Materials and methods

### 2.1 Experiment

#### 2.1.1 Microfluidic chip fabrication

Figure 1A shows a top-view picture of the microfluidic chip used in our experiments, which was fabricated with PDMS

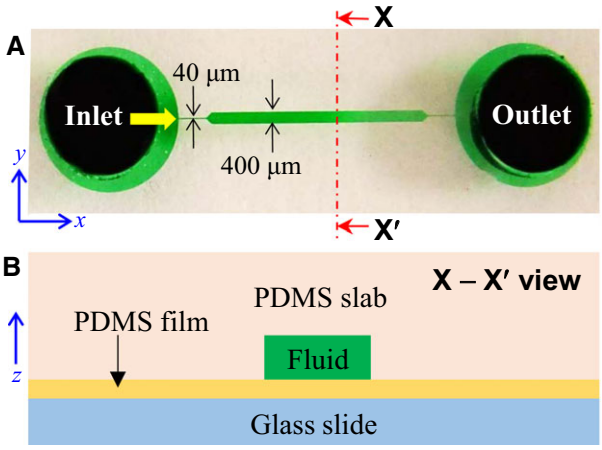


**Figure 1.** Top-view picture (A, the channel and reservoirs are filled with green food dye for clarity) and schematic cross-sectional view (B, not to scale) of the microfluidic chip used in experiments. The electrodes were assumed to be right in the center of the reservoirs in both experiment and simulation. The block arrow in (A) shows the direction of electroosmotic fluid flow.

using the standard soft lithography technique. The detailed fabrication procedure can be referred to our previous paper [43] and is skipped here. The chip has a 2 mm thick PDMS slab on top and a 1 mm thick glass slide at the bottom with a 10 μm thin PDMS film sandwiched between. This three-layer structure is schematically illustrated by the cross-sectional view in Fig. 1B. At the bottom side of the PDMS slab is the 25 μm deep microchannel, which is composed of a long straight section of 400 μm wide in the middle and a tapered 40 μm wide, 1 mm long constriction at each end. The total length of the microchannel is 1 cm. At the far end of each constriction is a 5 mm diameter reservoir for the fluid and sample supply. The radius of each corner at the inlet/outlet reservoir-microchannel junctions was measured to be 30 μm. This same value was used as the corner radius in the numerical model. It is important to note that the PDMS-PDMS configuration of the microchannel ensures uniform and identical surface properties for the walls that surround the fluid.

#### 2.1.2 Particle solution preparation and experimental methods

In order to study Joule heating effects on the fluid flow pattern, 520 nm diameter fluorescent polystyrene microspheres (Bangs Laboratories, Fishers, IN) were used as tracers and resuspended in 5 mM phosphate buffer solution. DC-biased AC electric voltages were applied through 0.5 mm diameter platinum electrodes in the inlet and outlet reservoirs. They were supplied using a function generator (33220A, Agilent Technologies, Santa Clara, CA) that was connected with a high-voltage amplifier (609E-6, Trek, Medina, NY). The AC voltage frequency was fixed at 1 kHz in experiments. Particle motion at the inlet/outlet reservoir-microchannel junctions

 

was monitored using an inverted microscope imaging system (Nikon Eclipse TE2000U, Nikon Instruments, Lewisville, TX) and recorded with a CCD camera (Nikon DS-Qi1Mc) at a rate of about 15 frames per seconds. The captured digital images were processed using the Nikon imaging software (NIS-Elements AR 2.30, Nikon Instruments). Prior to every test, the liquid heights in the two reservoirs were carefully balanced to minimize the effects of pressure-driven flow. Also, each test was run for no more than 1 min to avoid any significant backflow. It is important to note the temperature field does not necessarily reach the steady state within this time period in all tested cases due to the slow thermal diffusion across the chip [24]. However, the variations in the temperature and flow fields beyond 1 min have both been demonstrated to be small in a recent 3D trainset simulation [40].

## 2.2 Theory

In this section, we first present the 2D depth-averaged governing equations for the coupled electric charge, energy, and fluid transport involved in on-chip electroosmotic flows. Next, the computational domain for the microfluidic chip is described along with boundary conditions necessary for solving the governing equations. Finally, we present the numerical method with a table of parameters needed for modeling.

### 3.2.1 Governing equations

#### 3.2.1.1 Electric field

As PDMS can be considered to be electrically insulating, electric field is confined inside the fluid and governed by the quasielectrostatic equation [44] as follows:

$$\nabla \cdot (\sigma \mathbf{E} + i\omega \mathbf{D}) = 0, \tag{1}$$

where $\sigma$ is the electric conductivity of the fluid that is dependent on the concentration and mobility of ions dissolved therein [45], $\boldsymbol{E} = -\nabla\phi$ is the electric field with $\phi$ as the electric potential, $i$ is the imaginary unit, $\omega = 2\pi f$ is the angular frequency of the applied electric voltage with $f$ as the normal frequency, and $\boldsymbol{D} = \varepsilon \boldsymbol{E}$ is the electric field displacement with $\varepsilon$ as the fluid's electric permittivity. Note that the convection current has been assumed to be negligible when compared with the conduction current, $\boldsymbol{\sigma}\mathbf{E}$ [44]. We are using DC-biased AC electric fields with the AC frequency, $f$ (of 1 KHz), being much less than the charge relaxation frequency, $\sigma/2\pi\varepsilon$ (of MHz order [44]). This results in negligible effects of frequency on the electric field displacement, and hence Eq. (1) reduces to

$$\nabla \cdot (\sigma \mathbf{E}) = 0. \tag{2}$$

We follow the same analysis as in our previous papers [36, 40, 43] to solve only the DC component of electric field, $\boldsymbol{E}_{\mathrm{DC}}$. The method used to incorporate the AC component into the energy and flow equations will be discussed later. A depth-averaged analysis for Eq. (2) was done by the use of an asymptotic method described in Lin et al. [46] (see the Supporting Information for the detailed derivation). The resulting 2D equation for the DC electric field preserves its original form in 3D and is given by

$$\nabla_{\mathrm{H}} \cdot (\sigma \boldsymbol{E}_{\mathrm{DC}}) = 0, \tag{3}$$

where $\nabla_{\mathrm{H}}$ is the gradient along the $x$ and $y$ directions in the horizontal plain, and $\boldsymbol{E}_{\mathrm{DC}} = -\nabla\phi_{\mathrm{DC}}$ with $\phi_{\mathrm{DC}}$ being the DC electric potential.

#### 3.2.1.2 Temperature field

The applied electric field across the microchannel induces Joule heating in the fluid, especially strong inside the two constriction regions due to the locally amplified electric field. This heat generated within the fluid is diffused in all directions through the PDMS and glass substrates in three modes: (i) conduction from the bottom wall of the channel to the PDMS film and then the glass substrate (see Fig. 1B); (ii) conduction from the top and side walls of the channel to the PDMS slab, which is then removed by the natural convection on the top and side surfaces of the PDMS slab; (iii) natural convection on the top surface of the fluid in each reservoir. Hence temperature gradients are formed throughout the microfluidic chip. The steady-state time-averaged temperature field, $T$, in the fluid is governed by the energy equation [44]:

$$\rho C_{\mathrm{p}} (\boldsymbol{u} \cdot \nabla T) = \nabla \cdot (k \nabla T) + \sigma \left\langle \boldsymbol{E}^2 \right\rangle, \tag{4}$$

where $\rho$, $C_{\mathrm{p}}$, and $k$ are the mass density, heat capacity, and thermal conductivity, respectively, of the fluid, and $\mathbf{u}$ is the fluid velocity. The last term on the right-hand side of Eq. (4) is the time-averaged heat generation due to Joule heating (present only inside the fluid) where the contributions from the flow and concentration induced ion transport have been neglected [45]. By the use of dimensional analysis, we find that the thermal Peclet number, $\mathrm{Pe} = \mathrm{RePr}$ is smaller than 0.1 because the Reynolds number is $\mathrm{Re} \leq 0.01$ and the Prandtl number is $\mathrm{Pr} < 10$ under our experimental conditions [43, 44]. Therefore, the advection term in Eq. (4) can be dropped out leaving a purely heat conduction equation:

$$0 = \nabla \cdot (k \nabla T) + \sigma \boldsymbol{E}_{\mathrm{DC}}^2 \left(1 + r^2\right), \tag{5}$$

where the ratio of root mean squared AC field to DC field, $r$ (equivalent to the ratio of the imposed RMS AC voltage to DC voltage), is used to account for the effects of both AC and DC electric fields on Joule heating [36, 39, 40].

An asymptotic analysis of Eq. (5) yields the following 2D depth-averaged energy equation in the fluid (see the Supporting Information for the detailed derivation),

$$0 = k\nabla_{\mathrm{H}}^2 T + \sigma \mathbf{E}_{\mathrm{DC}}^2 \left(1 + r^2\right) - \frac{T - T_\infty}{d_{\mathrm{ch}}} \left( \frac{1}{R_{\mathrm{us}}} + \frac{1}{R_{\mathrm{ls}}} \right) \tag{6a}$$

$$R_{\mathrm{us}} = t_{\mathrm{us,PDMS}}/k_{\mathrm{PDMS}} + 1/h \tag{6b}$$

$$R_{\mathrm{ls}} = t_{\mathrm{ls,PDMS}}/k_{\mathrm{PDMS}} + t_{\mathrm{glass}}/k_{\mathrm{glass}} \tag{6c}$$

 

The last term on the right-hand side of Eq. (6a) accounts for the heat dissipation through the upper and lower substrates to the fluid (see Fig. 1B), where $T_\infty$ is the room temperature, $d_{ch}$ is the depth of the microchannel, and *Rus* and $R_{ls}$ are the equivalent thermal resistances offered by the upper and lower substrates to the fluid, respectively [47]. In the definitions of thermal resistances in Eqs. (6b) and (6c), $t_{us,PDMS}$ is the thickness of the PDMS slab (see Fig. 1B), $_{kPDMS}$ is the thermal conductivity of PDMS, $h$ is the natural convection coefficient, $t_{ls,PDMS}$ is the thickness of the PDMS film (see Fig. 1B), and $t_{glass}$ and $_{kglass}$ are the thickness and thermal conductivity of glass. Note that natural convection is considered only for the upper-substrate thermal resistance while an isothermal condition is used in the lower-substrate thermal resistance. The latter condition is based on the assumption that the bottom surface of the glass slide is in perfect contact with the large flat surface of the microscope stage whose temperature is fixed at the room temperature. This condition has been demonstrated in several recent numerical studies to match the experimental results well [24, 47]. It is also important to note that the fluid inside the reservoirs experiences a different upper-substrate thermal resistance, $R_{us}$, from that in Eq. (6b), where the thermal conductivity of PDMS, $k_{PDMS}$, should be replaced with the fluid thermal conductivity, $k$.

#### 3.2.1.3 Flow field

As noted earlier, the Reynolds number is much smaller than one in our experiments, so the flow field is governed by the continuity equation and the modified Stokes equations [44],

$$\nabla \cdot \boldsymbol{u} = 0 \tag{7a}$$

$$0 = -\nabla p + \nabla \cdot (\eta \nabla \boldsymbol{u}) + \langle \boldsymbol{f}_e \rangle \tag{7b}$$

where $p$ is the pressure, $\eta$ is the dynamic viscosity of the fluid. The time-averaged electrothermal body force, $\langle \mathbf{f}_e \rangle$, is equal to the sum of Coulomb force and dielectric force terms given by [48],

$$\langle \boldsymbol{f}_e \rangle = \left\langle \rho_e \boldsymbol{E} - 0.5 \boldsymbol{E}^2 \nabla \varepsilon \right\rangle \tag{8}$$

where $\rho_e$ is the free charge density given by Poisson's equation, $\rho_e = \nabla \cdot (\varepsilon \boldsymbol{E})$. A linear asymptotic analysis for Eq. (7a) and (7b) leads to the following 2D depth-averaged flow equations (see the Supporting Information for the detailed derivation),

$$\nabla_H \cdot \boldsymbol{u} = 0 \tag{9a}$$

$$0 = -\nabla_H p + \nabla_H \cdot (\eta \nabla_H \mathbf{u}) + \boldsymbol{f}_e - 3(\eta \boldsymbol{u} + \varepsilon \zeta_w \boldsymbol{E}_{DC}) / d_{ch}^2 \tag{9b}$$

$$f_e = \left(1 + r^2\right) \left[\nabla_H \cdot (\varepsilon \boldsymbol{E}_{DC}) \boldsymbol{E}_{DC} - 0.5 \boldsymbol{E}_{DC}^2 \nabla_H \varepsilon\right] \tag{9c}$$

Note that the effects of AC voltage on the electrothermal body force has been considered by the use of the AC to DC field ratio, $r$, in Eq. (9c) [36, 39–41]. This force is none zero due to the presence of gradients in fluid properties such as electric conductivity [through $\boldsymbol{E}_{DC}$ in Eq. (3)] and permittivity, which are caused by the Joule heating induced temperature gradients. The last term of Eq. (9b) is the additional body force that arises due to the depth-averaging with $\zeta_w$ being the wall zeta potential [46].

As mentioned earlier, the fluid flow field is visualized by tracking the motion of small fluorescent particles. The trajectories of these tracing particles are simulated by calculating their velocity, $\mathbf{U}_P$, as a vector sum of fluid velocity, $\boldsymbol{u}$, and electrophoretic particle velocity, $\mathbf{U}_{EP}$,

$$\mathrm{U}_P = \mathrm{u} + \mathrm{U}_{EP} \tag{10a}$$

$$\mathrm{U}_{EP} = \varepsilon \zeta_p \boldsymbol{E}_{DC} / \eta \tag{10b}$$

where $\zeta_p$ is the particle zeta potential. The influence of DEP on particle velocity has been neglected in Eq. (10a) because it is found in our simulation to be two orders of magnitude smaller than the fluid velocity. Other contributions to particle velocity due to, for example, Brownian, inertial and gravitational motions are also neglected [49].

### 3.2.2 Computational domain and boundary conditions

The coupled depth-averaged electric, temperature, and flow field equations, that is, Eqs. (3), (6a), (9a), and (9b), are solved simultaneously in the horizontal plain of the microfluidic chip that cuts the microchannel by half along its depth. Figure 2 shows the 2D computational domain that covers only one half of the chip due to symmetry. It has the fluid and PDMS subdomains where the latter is, however, solved only for the temperature field. Due to their high thermal and electric conductivities, platinum electrodes are considered to remain at constant temperature and electrical potential during the experiment and hence simply treated as holes with appropriate boundary conditions in the 2D simulation. The four boundaries of the computational domain in Fig. 2 are the microchannel sidewalls, electrode surfaces, outer walls of PDMS, and the symmetry line. The boundary conditions required to solve the coupled equations are summarized below except for the symmetry ones.

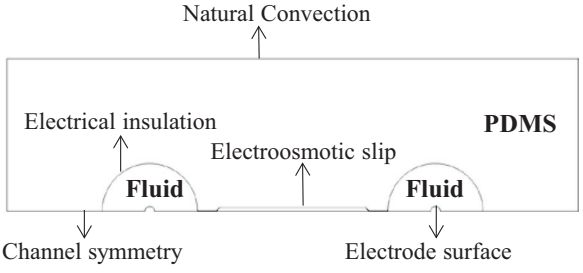


**Figure 2.** Computational domain for the 2D depth-averaged modeling of the electrokinetic microfluidic chip with important boundary conditions being highlighted.

 

#### 3.2.2.1 Electric field

Electric potential, $\phi_{DC} = \phi_{DC}^0$ , is applied on the inlet electrode surface where $\phi_{DC}^0$ is the applied DC voltage. On the other electrode surface $\phi_{DC} = 0$ (ground) is applied. Since the electric field is confined within the fluid subdomain, an electrically insulating condition, $\boldsymbol{n} \cdot (\sigma \nabla \phi_{DC}) = 0$, is imposed on all sidewalls of the microchannel where $\boldsymbol{n}$ denotes the unit normal vector.

#### 3.2.2.2 Temperature field

Due to the electrode's high thermal conductivity, we assume there is no temperature drop inside each electrode. Moreover, as the electrodes are each connected with the power supply via a large electrical board that remains at the room temperature, an isothermal condition, $T = T_\infty$ , is applied on the electrode surfaces. The condition of temperature continuity is applied by default in COMSOL at the interface of the fluid and PDMS subdomains. The outer walls of PDMS are exposed to atmosphere and hence experience a natural convection.

#### 3.2.2.3 Flow field

On the surface of electrodes, a no-slip condition, $\boldsymbol{u} = 0$, is applied because the local electric field is normal to its surface. As pressure driven flow is absent, an equal pressure needs to be applied to each of the reservoir. In our model, we choose one point each on the most left and right ends of the fluid subdomain (that lies on the line of symmetry) and apply the condition, $p = 0$. Since the electric double layer is very small (on the order of few nanometers in our experimental conditions) compared to the width of the microchannel, fluid motion can be modeled by using the well-accepted Smoluchowski electroosmotic slip velocity [1, 2], $\boldsymbol{u} = -\varepsilon \zeta_w \boldsymbol{E}_{DC}/\eta$, on the sidewalls of both the microchannel and the reservoirs.

### 3.2.3 Numerical method and material properties

Commercial finite element software package, COMSOL Multiphysics 5.1 (Burlington, MA) was used to carry out the numerical simulation. The 2D geometry in Fig. 2 was created using the "Geometry" feature. The modules of "Electrical currents," "Heat transfer in fluids," "Heat transfer in solids," and "Laminar flow" were coupled together to solve the governing equations, that is, Eqs. (3), (6a), (9a), and (9b). The function of "Streamline" was used to plot the streaklines of tracing particles via the velocity in Eq. (10a). In order to avoid singularities, sharp corners were filleted. The domain was meshed using approximately 120 000 free triangular elements. The number of elements was varied from 5000 to 120 000 and we found that the results were grid independent after approximately 60 000 elements. The constriction region was meshed extremely fine (with a maximum element size of 2 μm) compared to the mesh size at other regions because of the occurrence of high electric field, temperature, and fluid property gradients in the former. The model was solved using a nonlinear, segregated, iterative solver with appropriate damping factors to achieve a faster convergence. The whole process for one run took about 10 minutes in a standardly configured laptop (8 GB RAM, Intel i5 processor and 2 cores) while the previously developed 3D model required over 4 h in a supercomputing cluster (Clemson Palmetto, 400 GB of RAM and 24 core processor).

The temperature dependences of the fluid properties including electric conductivity, permittivity and viscosity were evaluated in our model using the following expressions [19, 22]

$$\sigma = \sigma_\infty \left[1 + \beta \left(T - T_\infty\right)\right] \tag{11a}$$

$$\varepsilon = \varepsilon_\infty \left[1 + \alpha \left(T - T_\infty\right)\right] \tag{11b}$$

$$\eta = 2.761 \times 10^{-6} \exp\left(1713/T\right) \tag{11c}$$

**Table 1.** Summary of parameters and material properties used for modeling [51, 52]

| Symbol | Value | Unit | Description |
|---|---|---|---|
| $T_\infty$ | 293 | K | Room temperature |
| $\sigma_\infty$ | 0.1 | S/m | Fluid electric conductivity at room temperature |
| $\varepsilon_\infty$ | $7.09 \times 10^{-10}$ | F/m | Fluid electric permittivity at room temperature |
| α | −0.0046 | 1/K | Temperature coefficient of fluid electric permittivity |
| β | 0.02 | 1/K | Temperature coefficient of fluid electric conductivity |
| $k$ | 0.61 | W/(m•K) | Thermal conductivity of fluid |
| $k_{PDMS}$ | 0.15 | W/(m•K) | Thermal conductivity of PDMS |
| $k_{glass}$ | 1.38 | W/(m•K) | Thermal conductivity of glass |
| $d_{ch}$ | 25 | μm | Depth of microchannel |
| $t_{us,PDMS}$ | 2 | mm | Thickness of PDMS slab |
| $t_{ls,PDMS}$ | 10 | μm | Thickness of PDMS film |
| $t_{glass}$ | 1 | mm | Thickness of glass slide |
| $h$ | 10 | W/(m$^2$•K) | Natural convection heat-transfer coefficient |
| $\zeta_w$ | −50 | mV | Zeta potential of walls |
| $\zeta_p$ | −80 | mV | Zeta potential of particles |
| ρ | 1000 | kg/m$^3$ | Mass density of fluid |

 

where $\sigma_\infty$ and $\varepsilon_\infty$ are the electric conductivity and permittivity of the fluid at room temperature $T_\infty$, and $\beta$ and $\alpha$ are their respective temperature coefficients. The values of these constants along with other parameters used in the model are given in Table 1. Note that the wall zeta potential, $\zeta_w$, was determined from the measured electroosmotic fluid velocity via the electric current monitoring method in a straight uniform microchannel [50]. The particle zeta potential, $\zeta_p$, was calculated from the electrokinetic particle velocity that was measured by tracking single particle motions in a straight uniform microchannel [14–16]. The heat transfer coefficient for natural convection, $h$, was estimated using the correlations from Incropera and DeWitt [51] to be 10 W/(m$^2$•K), which is consistent with the value used in previous studies [24, 47].

## 3 Results and discussion

Figure 3 shows the comparison of experimentally obtained superimposed images and numerically predicted particle streaklines at the interface of the inlet reservoir and microchannel for various 20 V DC-biased AC voltages. In each case the flow pattern is established soon after the electric voltage is supplied. At 450 V AC, the tracing particles mostly follow electric field lines and flow smoothly from reservoir to microchannel. Only those that travel near the channel centerline exhibit a slight bending, which is correctly captured by our simulation in Fig. 3A (bottom half). This phenomenon is not expected for a pure electroosmotic flow with uniform properties due to the similarity of flow and electric fields therein [53]. It is a consequence of electrothermal flow that arises from the action of electric field on Joule heating induced fluid inhomogeneities. This flow grows with the increase of AC voltage, leading to the formation of two small counterrotating vortices near the centerline of the channel entrance at 500 V AC (see Fig. 3B). Further increasing the AC voltage significantly enhances the fluid circulations as demonstrated in Fig. 3C for 600 V AC and Fig. 3D for 700 V AC. The experimentally observed variations in the size and location of electrothermal circulations with AC voltage are predicted with a good agreement for every case in Fig. 3.

The generation of electrothermal fluid circulations in electroosmotic entry flow can be explained by the numerically predicted fluid property and field contours in Fig. 4 for the case of 20 V DC-biased 600 V AC. The size mismatch between the reservoir and the microchannel (more precisely, the constriction section of the channel; see Fig. 1A) amplifies the electric field inside the microchannel as illustrated in Fig. 4A. This draws strong Joule heating in the constriction region and hence raises the local fluid temperature. However, as viewed from Fig. 4B, the fluid inside the reservoir remains slightly above room temperature. The resulting steep temperature gradients lead to highly nonuniform fluid properties at the reservoir-microchannel junction, e.g., electric permittivity decreases by approximately 10% (Fig. 4C) while electric conductivity increases by almost 50% (Fig. 4D) in the constriction. The action of electric field (both DC and AC) on these gradients in fluid properties induces the electrothermal body force, that is, $\mathbf{f}_e$ in Eq. (9c), at the channel entrance region. The magnitude of this force is higher near the channel walls (than the centerline, see Fig. 4E) and hence able to reverse the local fluid velocity (toward reservoir), yielding the electrothermal fluid circulations in Fig. 4F.

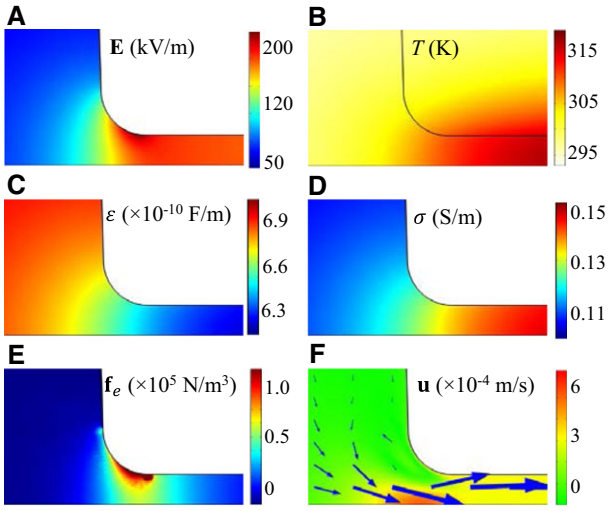


**Figure 4.** Illustration of numerically predicted contours of electric field (A), temperature field (B), electric permittivity (C), electric conductivity (D), electrothermal body force (E), and fluid velocity magnitude (F, arrows are velocity vector plots) at the inlet reservoir-microchannel junction under 20 V DC-biased 600 V AC.

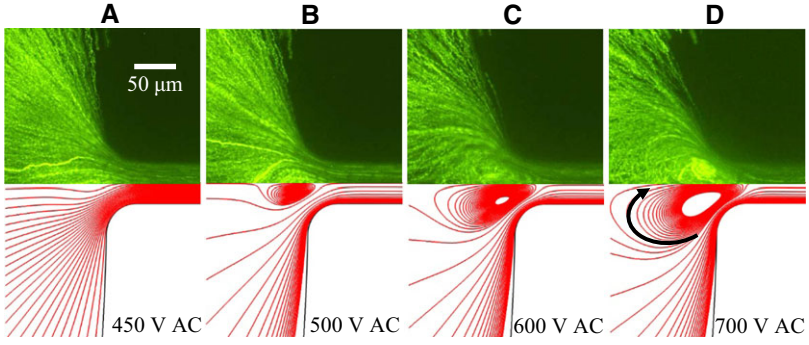


**Figure 3.** Comparison of experimentally obtained images (top half) and numerically predicted streaklines (bottom half) of 520 nm tracing particles at the inlet reservoir-microchannel junction under various 20 V DC-biased AC voltages: (A) 450 V AC (root mean squared), (B) 500 V AC, (C) 600 V AC, and (D) 700 V AC. The arrowed line in D indicates the direction of the electrothermal flow circulation. The direction of electroosmotic fluid flow is from left to right in all images while that of the tracing particles is opposite due to the dominance of particle electrophoresis over fluid electroosmosis.

 

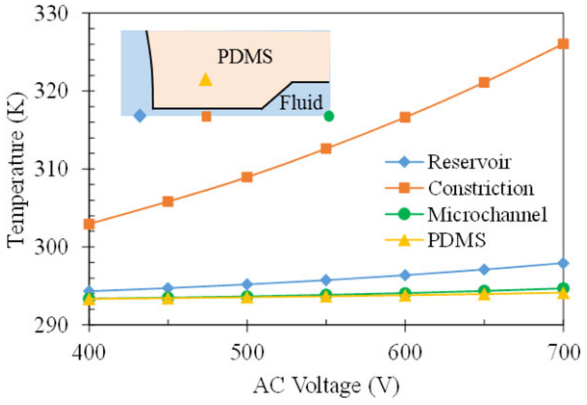


**Figure 5.** Numerically predicted temperature variations at four points of the computational domain (see their locations in the inset, not drawn to scale; refer also to Fig. 2) for various AC voltages with a fixed 20 V DC offset.

The growth of electrothermal fluid circulations at a higher AC voltage in Fig. 3 is attributed to the increase in Joule heating induced temperature gradients (and in turn fluid property gradients). This is demonstrated in Fig. 5, where the temperature variations at four points of the microfluidic chip (see their locations in the inset) are plotted for various AC voltages: (i) 200 μm ahead of the constriction inside the reservoir, (ii) center of the constriction, (iii) center of the microchannel, and (iv) 200 μm above the constriction inside the PDMS. The fluid temperature at the center of the constriction increases in a parabolic nature with increase in AC voltage. In contrast, the fluid temperature rise inside the reservoir is almost linear and much less than that in the constriction. This difference in temperature variation causes significantly increased temperature gradients at the reservoir-microchannel junction for higher AC voltages. However, the temperatures at the center of the microchannel and the PDMS both experience a very small increase with AC voltage. This indicates that Joule heating in the fluid is primarily rejected along the channel depth direction, especially through the glass slide at the bottom [24, 40]. In addition, the increase of corner radius at the reservoir-microchannel junction is found to reduce the local electric field intensity and hence slightly weaken the electrothermal flow circulation [40].

Electrothermal flow also occurs in electroosmotic exit flow from the microchannel to the outlet reservoir due to the same mechanism as noted above. The experimentally and numerically obtained particle streaklines at the outlet reservoir-microchannel junction are displayed in Fig. 6 for various 20 V DC-biased AC voltages. Similar to the electroosmotic entry flow in Fig. 3, fluid circulations appear at 500 V AC in the exit flow and become more prominent with the further increase in AC voltage. Moreover, the electrothermal flows in both locations point away from the channel at the near-wall region due to the local strong electrothermal body force (see Fig. 4E) and circulate back in the bulk fluid region (see the arrowed lines in Fig. 3D and Fig 6D). However, the centers of the two fluid vortices are shifted from near the channel centerline in the entry flow (Fig. 3) to near the channel walls in the exit flow (Fig. 6). These phenomena are all reasonably simulated by the 2D depth-averaged model.

## 4 Concluding remarks

This paper presents the first experimental and numerical studies of Joule heating effects on electroosmotic fluid entry from reservoir to microchannel in a polymer microfluidic chip. Electrothermal fluid circulations are observed to form at the reservoir-microchannel junction due to the action of the locally amplified electric field upon the Joule heating-induced gradients in fluid properties. Their influences on the electroosmotic entry flow grow with the increasing AC voltage when the DC voltage is fixed. Moreover, a depth-averaged theoretical analysis is performed for the transport equations, based on which a 2D numerical model is developed to understand the effects of Joule heating on fluid temperature and flow fields in electrokinetic microfluidic chips. This model takes into the account the heat dissipation and electroosmotic slip from/on the top and bottom microchannel walls without any assumption. It is found sufficient to predict the temperature field in both the fluid and substrate subdomains of the entire microchip. More importantly, it simulates accurately the size and position of the experimentally observed fluid vortices in electroosmotic flow at both the inlet and the outlet reservoir-microchannel junctions under various AC voltages. Due to the simple 2D nature, this modeling can be easily carried out in a laptop, which enables quick and efficient parametric studies for the optimal design and operation of electrically controlled microfluidic devices.

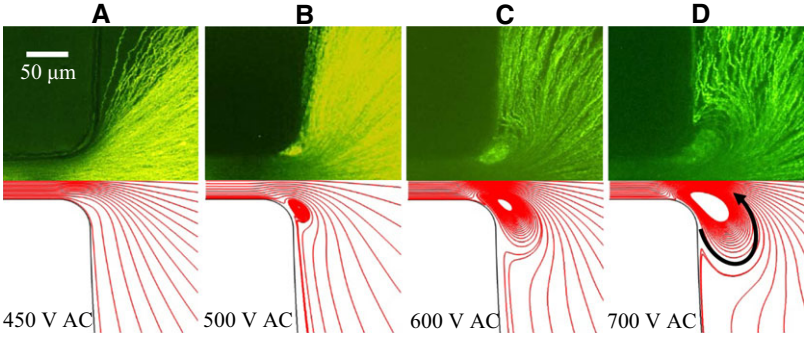


**Figure 6.** Comparison of experimentally (top) and numerically (bottom) obtained particle streaklines in electroosmotic exit flow from the microchannel to the outlet reservoir under various 20 V DC-biased AC (root mean squared) voltages: (A) 450 V AC, (B) 500 V AC, (C) 600 V AC, and (D) 700 V AC. The arrowed line in D indicates the direction of the electrothermal flow circulation. The direction of electroosmotic fluid flow is from left to right in all images.

*This work is partially supported by NSF under grant CBET-1150670 (X. X.), by University 111 Project of China under Grant B08046 (Y. S.), and by NSFC under grants 11272321 and 11572334 (G. H.). The support from the Open Fund of LNM (X. X. and G. H.) is also gratefully acknowledged.*

*The authors have declared no conflict of interest.*

## 5 References

[1] Li, D., *Electrokinetics in Microfluidics*, Elsevier Academic Press, Burlington, MA 2004.

[2] Marcos, Kang, Y. J., Ooi, K. T., Yang, C., Wong, T. N., *J. Micromech. Microeng.* 2005, *15*, 301–312.

[3] Chang, H. C., Yeo, L. Y., *Electrokinetically Driven Microfluidics and Nanofluidics*, Cambridge University Press, New York 2010.

[4] Bruin, G. J. M., *Electrophoresis* 2000, *21*, 3931–3951.

[5] Marcos, Ooi, K. T., Yang, C., Chai, J. C., Wong, T. N., *Int. J. Eng. Sci.* 2005, *43*, 1349–1362.

[6] Pethig, R., *Biomicrofluidics* 2010, *4*, 022811.

[7] Cetin, B., Li, D., *Electrophoresis* 2011, *32*, 2410–2427.

[8] Whitesides, G. M., Stroock, A. D., *Phys. Today* 2001, *54*, 42–48.

[9] Kang, Y., Li, D., *Microfluid. Nanofluidics* 2009, *6*, 431–460.

[10] Srivastava, S. K., Gencoglu, A., Minerick, A. R., *Anal. Bioanal. Chem.* 2010, *399*, 301–321.

[11] Jubery, T. Z., Srivastava, S. K., Dutta, P., *Electrophoresis* 2014, *35*, 691–713.

[12] Yang, R. J., Tseng, T. I., Chang, C. C., *J. Micromech. Microeng.* 2005, *15*, 254–262.

[13] Yan, D., Yang, C., Huang, X., *Microfluid. Nanofluidics* 2007, *3*, 333–340.

[14] Zhu, J., Hu, G., Xuan, X., *Electrophoresis* 2012, *33*, 916–922.

[15] Patel, S., Showers, D., Vedantam, P., Tzeng, T., Qian, S., Xuan, X., *Biomicrofluidics* 2012, *6*, 034102.

[16] Patel, S., Qian, S., Xuan, X., *Electrophoresis* 2013, *34*, 961–968.

[17] Harrison, H., Lu, X., Patel, S., Thomas, C., Todd, A., Johnson, M., Raval, Y., Tzeng, T., Song, Y., Wang, J., Li, D., Xuan, X., *Analyst* 2015, *140*, 2869–2875.

[18] Rathore, A. S., *J. Chromatogr. A* 2004, *1037*, 431–443.

[19] Cetin, B., Li, D., *Electrophoresis* 2008, *29*, 994–1005.

[20] Evenhuis, C. J., Haddad, P. R., *Electrophoresis* 2009, *30*, 897–909.

[21] Ghosal, S., *Electrophoresis* 2004, *25*, 214–228.

[22] Xuan, X., *Electrophoresis* 2008, *29*, 33–43.

[23] Voldman, J., *Annu. Rev. Biomed. Eng.* 2006, *8*, 425–454.

[24] Erickson, D., Sinton, D., Li, D., *Lab Chip* 2003, *3*, 141–149.

[25] Knox, J. H., *Chromatographia* 1988, *26*, 329–336.

[26] Andreev, V. P., Lisin, E. E., *Electrophoresis* 1992, *13*, 832–837.

[27] Gaš, B., Stedry, M., Kenndler, E., *Electrophoresis* 1997, *18*, 2123–2133.

[28] Xuan, X., Li, D., *Electrophoresis* 2005, *26*, 166–175.

[29] Xuan, X., Li, D., *J. Chromatogr. A* 2005, *1064*, 227–237.

[30] Tang, G., Yan, D., Yang, C., Gong, H. Q., Chai, C. K., Lam, Y. C., *Electrophoresis* 2006, *27*, 628–639.

[31] Samy, R, Glawdel, T., Ren, C. L., *Anal. Chem.* 2008, *80*, 369–375.

[32] Nakano, A., Luo, J., Ros, A., *Anal. Chem.* 2014, *86*, 6516–6524.

[33] Huang, K. D., Yang, R. J., *Electrophoresis* 2006, *27*, 1957–1966.

[34] Fu, L. M., Wang, H., Luo, W. B., Lin, C. H., *Microfluid Nanofluidics* 2009, *6*, 499–507.

[35] Gallo-Villanueva, R., Sano, M., Lapizco-Encinas, B., Davalos, R., *Electrophoresis* 2014, *35*, 352–361.

[36] Sridharan, S., Zhu, J., Hu, G., Xuan, X., *Electrophoresis* 2011, *32*, 2274–2281.

[37] Ramos, A., Morgan, H., Green, N. G., Castellanos, A., *J. Phys. D* 1998, *31*, 2338–2353.

[38] Gonzalez, A., Ramos, A., Morgan, H., Green, N. G., Castellanos, A., *J. Fluid Mech.* 2006, *564*, 415–433.

[39] Hawkins, B. J., Kirby, B. J., *Electrophoresis* 2010, *31*, 3622–3633.

[40] Kale, A., Patel, S., Hu, G., Xuan, X., *Electrophoresis* 2013, *34*, 674–683.

[41] Hawkins, B. G., Smith, A. E., Syed, Y. A., Kirby, B. J., *Anal. Chem.* 2007, *79*, 7291–7300.

[42] Lewpiriyawong, N., Yang, C., Lam, Y. C., *Microfluid. Nanofluidics* 2012, *12*, 723–733.

[43] Kale, A., Patel, S., Qian, S., Hu, G., Xuan, X., *Electrophoresis* 2014, *35*, 721–727.

[44] Casterllanos, A., Ramos, A., Gonzalez, A., Green, N. G., Morgan, H., *J. Phys. D* 2003, *36*, 2584–2597.

[45] Yoo, K., Shim, J., Dutta, P., *Biomicrofluidics* 2014, *8*, 064125.

[46] Lin, H., Storey, B. D., Santiago, J. G., *J. Fluid Mech.* 2008, *608*, 43–70.

[47] Zehavi, M., Boymelgreen, A., Yossifon, G., *Phys. Rev. Applied* 2016, *5*, 044013.

[48] Melcher, J. R., Taylor, G. I., *Annu. Rev. Fluid Mech.* 1969, *1*, 111–146.

[49] Green, N. G., Ramos, A., Morgan, H., *J. Phys. D* 2000, *33*, 632–641.

[50] Kale, A., PhD dissertation, *Joule heating Effects in Insulator-based Dielectrophoresis Microdevices*, Clemson University, Clemson SC 2015.

[51] Incorpera, F. P., DeWitt, D. P., *Fundamentals of Heat and Mass Transfer*, Wiley, New York, NY 1990.

[52] Lide, D. R., *CRC Handbook of Chemistry and Physics*, 90th edition, CRC press, Boca Raton, FL 2009.

[53] Cummings, E. B., Griffiths, S. K., Nilson, R. H., Paul, P. H., *Anal. Chem.* 2000, *72*, 2526–2532.

 